Materials & Design 210 (2021) 110058

Contents lists available at ScienceDirect

Materials & Design

journal homepage: www.elsevier.com/locate/matdes

On the sensitivity of the design of composite sound absorbing structures

V.H. Trinh [a], J. Guilleminot [b], C. Perrot [c,*]

[a] Faculty of Vehicle and Energy Engineering, Le Quy Don Technical University, 236, Hoang Quoc Viet, Ha Noi, Viet Nam
[b] Department of Civil and Environmental Engineering, Duke University, Durham, NC 27708, USA
[c] MSME, Univ Gustave Eiffel, CNRS UMR 8208, Univ Paris Est Creteil, F-77454 Marne-la-Vallée, France

HIGHLIGHTS

- Sound absorption can be tailored by using optimized composite panels.
- Global sensitivity indices are computed through Monte-Carlo and spectral approaches.
- Sensitivity functions are related to sound absorption resonance behaviors.
- Foam microstructural parameters are generally found to be the most influential ones.

GRAPHICAL ABSTRACT

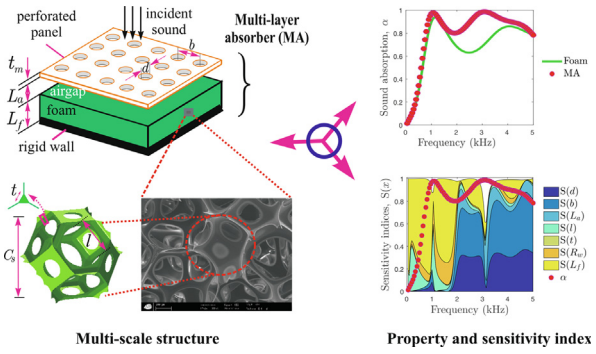

ARTICLE INFO

Article history:
Received 1 May 2021
Revised 24 July 2021
Accepted 19 August 2021
Available online 20 August 2021

Keywords:
Multi-layer absorber
Membrane
Foam
Sound absorption
Perforated panel
Optimization
Global sensitivity
Polynomial chaos expansions

ABSTRACT

The acoustic properties of composite structures made of a perforated panel, an air gap, and a porous layer, can be studied numerically by a combined use of ad hoc optimization and sensitivity analysis methods. The methodology is briefly described and is systematically applied to a series of multi-layer configurations under manufacturing constraints. We specifically consider a foam layer of constant thickness presenting three different degrees of reticulations (pore opening). For each foam layer, the optimal geometrical parameters of the perforated panel and the cavity depth maximizing sound absorption under normal incidence are determined, together with the corresponding sensitivity indices. The simulation results are found in good agreement with interpretations and experimental data provided elsewhere. From a general perspective, the framework can be used to identify the most influential parameters within multiscale settings for acoustics studies, hence enabling robust design under material and microstructural uncertainties for instance.

1. Introduction

The sound attenuation of compressional waves in layered porous structures is an important engineering physics topic that has led to various innovative applications in aeronautical, construction, and transport industries. The study of wave propagation in saturated porous media started with the phenomenological approach of Biot [1–7]. Later on, important progress was made by having recourse to homogenization theory for periodic structures with compressible and incompressible fluids [8–10]. Decisive advantages of this framework include the integration of the local point equations which govern wave propagation in the exact geometry, and the ability to derive boundary value problems at leading orders. This approach has paved the way for the construction of

* Corresponding author.
E-mail addresses: hai.tv@lqdtu.edu.vn (V.H. Trinh), johann.guilleminot@duke.edu (J. Guilleminot), camille.perrot@univ-eiffel.fr (C. Perrot).

https://doi.org/10.1016/j.matdes.2021.110058
0264-1275/

numerical models that, while compatible with a phenomenological description, account for an explicit description of the microstructure [11–16]. In order to reduce the computational cost associated with the prediction of the microstructure-dependent macroscopic parameters that are fed into a phenomenological theory, Doutres et al. proposed a more direct method which consists in conducting a series of laboratory measurements on samples presenting different microstructural features [18,19].

In order to achieve robust design, one may seek to better understand the statistical correlations between macroscopic parameters [20], or to predict the sensitivity of these parameters to microstructural properties [21] (see [22] for a combination of both strategies). Alternatively, one can consider optimization studies based on forward numerical simulations; see [23–26] for various applications involving additive manufacturing techniques and biomaterials, respectively. In classical robust engineering design, the main issue is to clarify how the variability associated with the model inputs affects the model outputs. Sensitivity analysis is also intended to determine which input parameters contribute the most to output variabilities (and as a corollary, which parameters can be considered insignificant for the case under consideration) and to estimate parameter interactions; [20] for an application in acoustics. Because in the classical semi-phenomenological approach the macroscopic parameters are inter-dependent, a multi-scale procedure has to be implemented to link the macroscopic response to the microstructure morphology, at the expense of the computational time. A way to circumvent this difficulty is to use a surrogate model to connect microstructure with transport parameters and account for the microstructure effects solely by a set of algebraic equations. Several studies have used this approach based on semi-empirical [18,19] or feedback shift correction techniques [23,26]. To our knowledge, no such unified approach has been presented for the robust design of composite sound absorbing structures including a porous material, an air gap, and a perforated panel. These elements, however, turn out to be the most appropriate ones for the sound absorption involved in industrial systems. These are the elements we used in our multi-scale robust design model.

In the case of multi-layer structures (see Chapter 11 in [27]), prototypical configurations include a perforated panel (PP) and a porous layer, separated by an air gap. Other configurations include the use of panels composed of a parallel arrangement of different quarter-wavelength resonators designed to be impedance matched at selected frequencies, e.g, optimally designed panels to the limit imposed by causality [28] or, in a similar way, optimized absorbers based a periodic array of varying cross-section waveguides, each of them being loaded by Helmholtz resonators with graded dimensions [29]. For a given frequency range, the design of relevant geometrical parameters can be achieved under constraints related to the perforation diameter in the covering panel for instance. Several recent contributions have addressed the optimization of acoustic properties for composite structures; see [25, 31–34]. In these works, various inner layers were considered, including metal foams [30], polymer fibrous layers [25,30], and micro-perforated panels with and without airgaps. Sound absorption optimization was addressed for wide bands (for instance, [2000 6000] [Hz] in [30,32]) or at low frequency (such as 400 [Hz] in [34]), by having recourse to various optimization techniques (such as a cuckoo search algorithm [30] or analytical methods [32]) or by tuning some factors in experiments [34]. However, works addressing optimization and robustness considerations simultaneously remain relatively scarce. In general, the influence of random parameters (modeling geometrical uncertainties for instance) on the acoustic performance of single- or multi-layer absorbers can be characterized by means of sensitivity analyses (SA). The latter essentially aim to quantitatively assess dependencies between the inputs and outputs of a selected model and allow one to rank model inputs in terms of their impacts on outputs of interest (see [35], Part IV Volume II, for reviews). Such calculations were conducted on acoustic porous models in Refs. [22,20,36,21], for instance. For single-layer absorbers (consisting of foam materials for example), previous works have considered macroscopic parameters (such as transport and mechanical buckling properties) as uncertain parameters, and acoustic characteristics (including acoustic absorption or surface impedance) as quantities of interest. The SA results indicated that resistivity is, in fact, the most influential parameter—regardless of whether input parameters are assumed correlated or statistically independent. From a technical standpoint, both the Sobol method and the Fourier Amplitude Sensitivity Test (FAST) were used to estimate sensitivity indices and led to consistent findings. Sensitivity analyses for moderately- to highly-reticulated polyurethane foams were performed in [21]. It was shown that in this case, the strut length is the dominant parameter as (i) it has a substantially impact on three important macroscopic non-acoustic parameters (namely, the airflow resistivity or viscous permeability, and the thermal and viscous characteristic lengths), and (ii) it generates large variability in the sound absorption coefficient. In the case of layered composite panels, the main acoustic responses (i.e. reflection, echo reduction, and transmission loss) over frequencies were selected as indicators for SA in [37,38], and it was shown that the Poisson's ratio and thickness of the coating are the most influential parameters for the reflection and transmission losses. In [38], the forward mapping was evaluated on surrogate models for semi-analytical laws, based on finite element computations.

Following the previous discussion, this work has two major objectives. The first one is to apply a numerical optimization technique to determine geometrical parameters of composite structures which maximize sound absorption at normal incidence under given constraints. The second one is to determine the sensitivity of the design to geometrical parameters. The Transfer Matrix Method is used to predict the sound absorption of the multilayered structures stacked in series. In this approach, the perforated plate, the cavity depth, and the porous layer are addressed separately (each layer being related to the corresponding geometrical factors). This paper is organized as follows. Section 2 provides an overview of acoustical models for multi-layer absorbers, based on semi-analytical relationships. In Section 3, we present the mathematical formulation for design optimization and sensitivity analysis. The approach is subsequently deployed on multi-layer absorbers in Section 4. In addition to quantitative results, we also provide physical insight to support key findings. Conclusions and perspectives are finally provided in Section 5.

2. Acoustical models of multi-layer absorbers

In this section, we present acoustic models for multi-layer absorbers including a perforated panel, a cavity (i.e., airgap), and a membrane foam layer. Such a configuration is shown in Fig. 1 where details about geometrical parameters for the inner components are also indicated. For the PP,

2.1. Model of micro-perforated facing and air layer

The PP can be considered as a lattice of short narrow tubes. Distances between these tubes are typically larger than their diameters, but remain small as compared to the wavelength of the impinging sound wave. A comprehensive review of the different perforated plate models, including the comparison of models used in the literature for different geometries of duct discontinuities or perforations, has been proposed by Jaouen and Chevillotte [39].

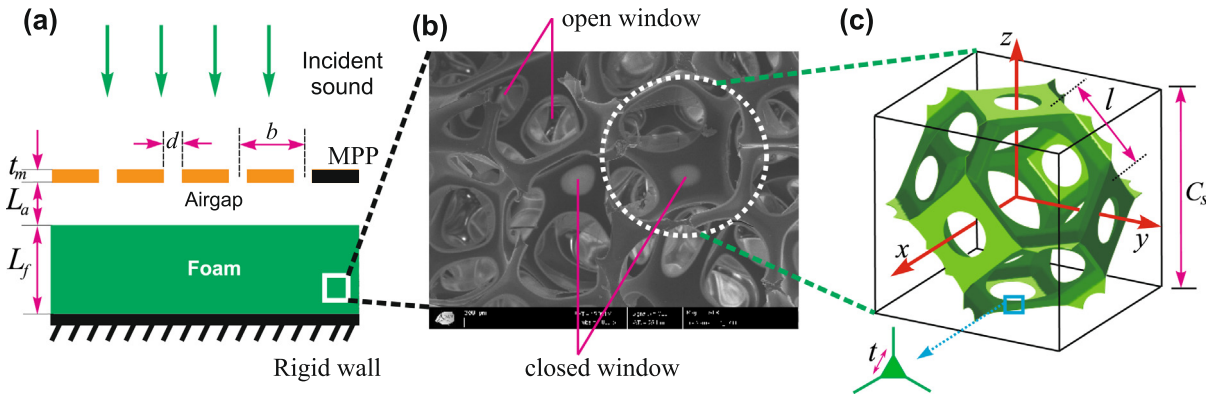

Fig. 1. (a) Multi-layer absorber configuration with a detailed description of all geometric parameters for the inner components. Here, t_m, L_a, and L_f are the thickness of the PP, airgap thickness, and foam layer thickness respectively. (b) Microstructure of the real (as-processed) foam. (c) Idealized periodic unit cell based on a C_s-size Kelvin model. The edge size and length of the ligaments or struts are denoted by l and t, respectively.

These comparisons allowed them to obtain two results. First, the mode-coupling at the discontinuity between two ducts or a perforated plate and air is negligible for low frequencies (when the wave number in air times the inner radius of the smallest duct or perforation radius is much smaller than one). Second, by using a length correction accounting for the line flow distortion around the aperture of the perforation to quantify the sound radiation effect of a perforation, they could verify that all consistent models depend both on a function of the square root of the perforation ratio and on the thickness of the plate. Therefore, in the perforated panel model, the periodicity of the perforations and the symmetry of the sound excitation (plane waves) imply that the linear acoustic problem at large wavelengths can be solved by studying only one pattern. The sound propagation in one pattern is considered to behave independently from its neighbors as the pattern dimensions are much smaller than the acoustic wavelength. In other words, week interaction between the evanescent modes inside and outside the perforation is assumed. Here, the Maa model is used to account for the effects of the perforated plate. At normal incidence, the wave motion in all the short tubes is in phase and additive. The relative acoustic impedance of the PP can be calculated as [40,41]

$$Z_M = \left[\frac{32\eta t_m}{d^2 p}\left(\sqrt{1+\frac{k_p^2}{32}}+\frac{\sqrt{2}k_p d}{8t_m}\right)\right] + j\omega\left[\frac{t_m}{p}\left(1+\frac{1}{\sqrt{9+k_p^2/2}}+\frac{0.85d}{t_m}\right)\right], \quad (1)$$

where

- η is the kinematic viscosity of air;
- d denotes the diameter of the hole;
- b represents hole spacing; and
- t_m is the thickness of the perforated panel (see Fig. 1a).

In addition, $\omega = 2\pi f$ denotes the angular frequency, p is the perforation ratio (given by $p = \pi d^2/4b^2$ for a square array), and $k_p = d/2\sqrt{\omega\rho_0/\eta}$ is the perforate constant which is proportional to the ratio of the perforation radius to the viscous boundary layer thickness inside the holes, with ρ_0 denoting the density of the saturating fluid (i.e., air). As shown in Ref. [41], the maximum error of the approximate formula (1) valid for all k_p values is 6% (at some k_p values between 1 and 10) compared to the exact value from Lord Rayleigh [42] and Crandall [43]. The limiting values of Z_M (exact asymptotic expressions) for small and large values of k_p were also given by Crandall when $k_p < 1$ and $k_p > 10$; see also Eq. (3) of [41].

The acoustic impedance of the rigidly backed air gap with depth L_a behind the PP layer (see Fig. 1a) is given by [27,41]

$$Z_A = -jZ_0 \cot(k_a L_a), \quad (2)$$

where $Z_0 = \rho_0 c_0$ is the acoustic impedance of air, and $k_a = \omega/c_0$ is the wave number in the air and c_0 is the speed of sound.

2.2. Multiscale model of a foam layer

In the equivalent fluid approach [3,7,4], the air in a rigid porous medium is replaced by an equivalent fluid characterized by an effective density and an effective bulk modulus. The main idea is to represent the frequency-dependant response functions of the porous material by an approximate but robust semi-phenomenological description, relying on a limited set of measurable macroscopic transport parameters, characterizing the essential physics of visco-thermal interactions. These effective properties account for the visco-inertial and thermal interactions with the frame and are given, according to the Johnson-Champoux-Allard (JCA) equivalent fluid model, by

$$\rho(\omega) = \rho_0\left(\alpha_\infty + \frac{\phi\sigma}{j\omega\rho_0}\sqrt{1+\frac{j\omega}{\nu}\frac{2\alpha_\infty\eta}{\Lambda^2\phi\sigma}}\right), \quad (3)$$

$$K(\omega) = \frac{\gamma P_0}{\phi}\left\{\gamma+(\gamma-1)\left[\frac{8\nu}{j\omega\Lambda'^2}\left(1+\sqrt{1+\frac{j\omega}{\nu}\frac{2\alpha_\infty\eta}{\Lambda^2\phi\sigma}}\right)\right]^{-1}\right\}^{-1}, \quad (4)$$

where ρ_0 is the ambient air density, $\kappa = \gamma P_0$ is the air adiabatic bulk modulus, P_0 is the atmospheric pressure, γ is the specific heat ratio, and $\nu = \eta/\rho_0 = P_r\nu$, with P_r the Prandtl number. The following parameters provide the inputs of this semi-phenomenological model at macro-scale:

- the porosity, ϕ, is the fluid volume fraction of the porous material;
- the static flow resistivity, σ, is related to the classical static viscous permeability, k_0, by $k_0 = \eta/\sigma$;
- the viscous characteristic length, Λ, is a parameter introduced by Johnson et al. [3] that can be interpreted as a weighted volume-to-surface ratio and accounts for the throat region of the porous structure;

- the high-frequency tortuosity, α_∞, reflects the dispersion of the microscopic velocity field around the mean macroscopic value for the case of an inviscid fluid (when $\omega \to \infty$);
- the thermal characteristic length, $\Lambda\prime$, is the generalized hydraulic radius, that is, twice the fluid volume in the porous structure divided by its surface area.

In what follows, these macroscopic parameters are estimated from semi-empirical equations based on the geometric parameters of the foam [19]:

$$\phi = 1 - \frac{2\sqrt{3}-\pi}{\sqrt{2}}\left(\frac{t}{l}\right)^2, \tag{5}$$

$$\Lambda\prime = \frac{8\sqrt{2}l}{3} \times \frac{1-\phi}{1+2\sqrt{3}-R_w\left[1+2\sqrt{3}-4\pi t/\left(\sqrt{3}l\right)\right]}, \tag{6}$$

$$\Lambda = \frac{\Lambda\prime}{1.55}\left(\frac{1}{R_w}\right)^{-0.6763}, \tag{7}$$

$$\alpha_\infty = 1.05\left(\frac{1}{R_w}\right)^{0.3802}, \tag{8}$$

$$\sigma = 128\eta\left(\frac{3\pi t}{8\sqrt{2}l^2}\right)^2\left(\frac{1}{R_w}\right)^{1.1166}. \tag{9}$$

In the equations above, l and t denote the length and thickness of the struts, respectively; $R_w \in [0,1]$ is the reticulation rate (i.e., the membrane content, see Fig. 1b) in the foam layer. The cases $R_w = 0$ and $R_w = 1$ correspond to fully closed-cell and fully open-cell foams, respectively. In this model, the purely geometrical macroscopic parameters ϕ and $\Lambda\prime$ are derived from analytical calculations, whereas the general structure of the equations used to determine Λ, α_∞, and σ follows exact calculations in idealized situations from which the values of the coefficients and of the exponents were fitted against experimental data. It should be noticed that these morphological parameters can be estimated by using scanning electron microscope and optical images of the foam microstructure. The wave number k_c and characteristic impedance Z_c for the homogeneous layer can then be estimated from the JCA equivalent fluid model as

$$k_c(\omega) = \omega\sqrt{\frac{\rho(\omega)}{K(\omega)}}, \quad Z_c(\omega) = \sqrt{\rho(\omega)K(\omega)}. \tag{10}$$

2.3. Sound absorption performance of multi-layer absorbers

Applying the transfer matrix method [27,44], the total transfer matrix T_{total} of a multi-layer absorber (MA) can be obtained from the individual transfer matrices of the inner layers as follows:

$$T_{\text{total}} = \begin{bmatrix} T_{11} & T_{12} \\ T_{21} & T_{22} \end{bmatrix} = T_m T_a T_f, \tag{11}$$

where T_m, T_a, and T_f are the transfer matrices of the single PP, air gap, and foam layers, respectively. These matrices are given by

$$T_m = \begin{bmatrix} 1 & Z_M \\ 0 & 1 \end{bmatrix}, \tag{12}$$

$$T_a = \begin{bmatrix} \cos(k_a L_a) & jZ_0 \sin(k_a L_a) \\ \frac{j}{Z_0}\sin(k_a L_a) & \cos(k_a L_a) \end{bmatrix}, \tag{13}$$

and

$$T_f = \begin{bmatrix} \cos(k_c L_f) & jZ_c \sin(k_c L_f) \\ \frac{j}{Z_c}\sin(k_c L_f) & \cos(k_c L_f) \end{bmatrix}. \tag{14}$$

The normal incidence sound absorption coefficient (SAC) of a multi-layer absorber, denoted by $\alpha(\omega)$, is calculated as

$$\alpha(\omega) = \frac{4\Re(Z_T/Z_0)}{\left[1+\Re(Z_T/Z_0)\right]^2 + \left[\Im(Z_T/Z_0)\right]^2}, \tag{15}$$

where $\Re$ and $\Im$ denote the real and imaginary parts of a complex number, Z_T is the surface impedance of the multi-layer absorber. The parameter Z_T can be estimated as $Z_T = T_{11}/T_{21}$, where T_{11} and T_{21} are defined in Eq. (11).

In practice, the mean sound absorption coefficient α_A over a specific range of frequencies is often introduced in order to estimate the acoustic performance of an absorber in dedicated applications. This factor can be calculated as

$$\alpha_A = \frac{1}{N_f}\sum_{i=1}^{N_f}\alpha(\omega_i), \tag{16}$$

where N_f is the number of discrete angular and frequencies $\{\omega_i\}_{i=1}^{N_f}$ in the range of interest $[f_{\min}, f_{\max}]$ (see Section 4.1 and also Ref. [23] for two illustrative examples for sound absorption targets at low and high frequencies).

3. Methodology for sensitivity analysis and design optimization

In this section, we present a methodology pertaining to the optimization of multi-layer absorbers (that is, we seek a configuration for the multi-layer absorber that exhibits desired target properties). We specifically consider the maximization of the sound absorption coefficient $\alpha(\omega)$ at a given frequency ω, or the maximization of the mean sound absorption coefficient α_A. In order to derive the formulation, let $\boldsymbol{x}$ be the D-dimensional vector of geometrical design parameters, and let J denote a relevant cost function (which is the objective function representing the property to be maximized). In the present work, we consider a cost function related to the sound absorption coefficient (described in Section 2.3), namely

$$J(\boldsymbol{x}) = \alpha_A(\boldsymbol{x}), \tag{17}$$

or

$$J(\boldsymbol{x}) = \alpha(\omega;\boldsymbol{x}), \tag{18}$$

where $\alpha(\omega;\boldsymbol{x})$ denotes the sound absorption coefficient estimated at point $\boldsymbol{x}$ (in the design space) and at frequency ω (using Eq. (15) and the geometry parameterized by $\boldsymbol{x}$). Notice that the dependence on the frequency is omitted in the equation above, for the sake of notational convenience. For a single-layer absorber, one may consider $\boldsymbol{x} = (t_m, d, b, L_a)^{\mathsf{T}}$ for instance (in which case $D = 4$), where the parameters t_m, d, b, and L_a are shown in Fig. 1. The design space is denoted by $S \subset \mathbb{R}^D$ and is typically defined through inequality constraints, that is:

$$S = \{\boldsymbol{x} | \boldsymbol{l}_b \leqslant \boldsymbol{x} \leqslant \boldsymbol{u}_b\}, \tag{19}$$

where inequalities hold component-wise, and $\boldsymbol{l}_b$ and $\boldsymbol{u}_b$ are two deterministic vectors in $\mathbb{R}^D$ whose components are denoted by $l_{b,i}$ and $u_{b,i}$, respectively. The vectors $\boldsymbol{l}_b$ and $\boldsymbol{u}_b$ represent bounds on design parameters and are introduced to reflect manufacturing constraints for instance. For latter use, we write S as the cartesian product

$$S = \prod_{i=1}^{D} I_i, \tag{20}$$

where $I_i = [l_{b,i}, u_{b,i}]$ defines the admissible set for design variable x_i. Finally, inequality constraints between design parameters are formally written as $\boldsymbol{h}(\boldsymbol{x}) \geqslant \boldsymbol{0}$, where $\boldsymbol{h}$ is a vector with values in $\mathbb{R}^{n_{ic}}$ and $\boldsymbol{0}$ is the null vector.

The approach builds upon two ingredients, namely (i) variance-based sensitivity analysis, which is used to determine the influence of design parameters on the quantity of interest (here, the cost function J), and (ii) an optimization method able to handle the non-convexity of the cost function in acoustical design. These components are reviewed in the next sections.

3.1. Variance-based sensitivity analysis

Following the preceding introduction, we consider the mapping $\boldsymbol{x} \mapsto J(\boldsymbol{x})$ from S into $[0,1]$, where $\boldsymbol{x}$ denotes the vector of design variables and J is the objective function. A global sensitivity analysis aims to characterize the influence of design parameters on J and enables, in particular, the identification of the most influential variables. To this end, a probabilistic interpretation is introduced where uncertainties on $\boldsymbol{x}$ are propagated through the model and contributions to the variance exhibited by the now stochastic quantity of interest are analyzed through so-called sensitivity indices. Interested readers are referred to Part IV in the Handbook on Uncertainty Quantification [35] (and in particular, Chapter 34 for the material presented below) for a review, for instance.

We assume that uncertainties on $\boldsymbol{x}$ are modeled by a random variable $\boldsymbol{X} \sim P_{\boldsymbol{X}}$, where $P_{\boldsymbol{X}}$ denotes the probability distribution of $\boldsymbol{X}$. It is commonly assumed that the components $\{X_i\}_{i=1}^D$ of $\boldsymbol{X}$ are statistically independent, in which case

$$P_{\boldsymbol{X}} = \bigotimes_{i=1}^{D} P_{X_i}, \tag{21}$$

where P_{X_i} denotes the (marginal) probability measure of X_i with support I_i. In order to ensure well-posedness, we further assume that J is square-integrable:

$$\int_{\mathbb{R}^D} J(\boldsymbol{x})^2 P_{\boldsymbol{X}}(d\boldsymbol{x}) < +\infty. \tag{22}$$

Following the notation introduced by Owen [45], the ANOVA (or Sobol') decomposition of J then reads as [46]

$$J(\boldsymbol{x}) = \sum_{u \subseteq \mathscr{I}} J_u(\boldsymbol{x}_u), \tag{23}$$

where $\mathscr{I} = \{1, \ldots, D\}$ denotes an index set, u is a so-called *set of factors*, J_u is the *effect* corresponding to u, and the notation $\boldsymbol{x}_u$ designates the vector $\left(x_{i_1}, \ldots, x_{i_{|u|}}\right)^{\mathsf{T}}$ for $u = \{i_1, \ldots, i_{|u|}\} \subseteq \mathscr{I}$, with $|u|$ the cardinality of u (likewise, the notation $\boldsymbol{X}_u$ denotes the random variable $\left(X_{i_1}, \ldots, X_{i_{|u|}}\right)^{\mathsf{T}}$). The effects are defined recursively as

$$J_u(\boldsymbol{x}_u) = \int_{\mathbb{R}^{D-|u|}} J(\boldsymbol{x})\, P_{\boldsymbol{X}_{u^c}}(d\boldsymbol{x}_{u^c}) - \sum_{v \subset u} J_v(\boldsymbol{x}_v), \tag{24}$$

where u^c is the complementary set $\mathscr{I} \setminus u$ and $v \subset u$ indicates that v is a proper subset of u. An effect corresponding to a singleton, $u = \{i\}$ with $i \in \mathscr{I}$, characterizes the main effect associated with variable x_i, while effects defined for subsets of factors having a cardinality greater than 1 measure interaction effects amongst relevant variables. The effect $J_\varnothing$ defined by taking the set of factors as the empty set is given by

$$J_\varnothing = \int_{\mathbb{R}^D} J(\boldsymbol{x})\, P_{\boldsymbol{X}}(d\boldsymbol{x}), \tag{25}$$

which allows one to define the variance of J as

$$\sigma^2 = \int_{\mathbb{R}^D} \left(J(\boldsymbol{x}) - J_\varnothing\right)^2 P_{\boldsymbol{X}}(d\boldsymbol{x}). \tag{26}$$

It follows, using Eq. (23) and owing to the orthogonality of the effects, that

$$\sigma^2 = \sum_{u \subseteq \mathscr{I}, u \neq \varnothing} \sigma_u^2, \tag{27}$$

where

$$\sigma_u^2 = \int_{\mathbb{R}^{|u|}} J_u(\boldsymbol{x}_u)^2\, P_{\boldsymbol{X}_u}(d\boldsymbol{x}_u) \tag{28}$$

is the variance component associated with $u \neq \varnothing$. The closed sensitivity index is subsequently defined as

$$\tau_u^2 = \sum_{v \subseteq u} \sigma_v^2 \tag{29}$$

and can be normalized to yield the global sensitivity index

$$\widehat{\tau}_u^2 = \frac{\tau_u^2}{\sigma^2}. \tag{30}$$

The Sobol' (first-order) sensitivity index related to the main effect $J_{\{k\}}$ is denoted by

$$\mathrm{S}_k = \widehat{\tau}_{\{k\}}^2, \tag{31}$$

where $\widehat{\tau}_{\{k\}}^2$ is given by Eq. (30). The total sensitivity index associated with variable x_k is finally defined as the sum of all Sobol' indices associated with factors involving the index k, and is denoted by ST_k:

$$\mathrm{ST}_k = \sum_{u \in \mathscr{I}_k} \widehat{\tau}_u^2, \tag{32}$$

where the set of factor subsets is defined as

$$\mathscr{I}_k = \left\{u \subseteq \mathscr{I}, u \neq \varnothing | \exists j \in \{1, \ldots, |u|\}, u_{i_j} = k\right\}. \tag{33}$$

With a view towards the evaluation of Sobol' indices through statistical sampling, it is convenient to rewrite the closed sensitivity index τ_u^2 as (see Section 2.1 in [45])

$$\tau_u^2 = \mathrm{Var}\{\mathbb{E}\{J(\boldsymbol{X}) | \boldsymbol{X}_u = \boldsymbol{x}_u\}\}. \tag{34}$$

In practice, one can resort to Monte-Carlo simulations to compute indices of interest (see Refs. [46–48]), or use a spectral decomposition as proposed by Sudret [49]. The former approach is usually more intensive from a computational standpoint, since numerous calls to the model are necessary to ensure the convergence of the statistical estimators. Several strategies were proposed to partially circumvent this issue, such as the use of nonparametric kernel regression [50] or learning techniques [51]. In the latter approach, a surrogate model based on a generalized polynomial chaos expansion is built to approximate the mapping $\boldsymbol{x} \mapsto J(\boldsymbol{x})$. This enables the derivation of Sobol' indices in closed-form at the additional expense of the computation of the coefficients in the chaos representation. In this work, we use the spectral decomposition approach to evaluate the sensitivity indices (see the aforementioned reference). In all subsequent computations, Monte Carlo simulations were also conducted to define reference results and characterize the convergence of the spectral decomposition.

3.2. Particle swarm optimization for sound absorption applications

We now turn to the optimization strategy for sound absorption coefficients. The problem is stated as: Find $\boldsymbol{x}_{\mathrm{opt}} \in S$ such that

$$\boldsymbol{x}_{\mathrm{opt}} = \arg\max_{\boldsymbol{x} \in S} J(\boldsymbol{x}), \tag{35}$$

subject to the constraint

$$h(\boldsymbol{x}) = x_3 - x_2 \geqslant 0, \tag{36}$$

where $\boldsymbol{x}$ gathers the design variables t_m (thickness of the perforated panel), d (diameter of the hole), b (hole spacing), and L_a (airgap thickness); see Fig. 1. Notice that the above inequality constraint is introduced to ensure that $b \geqslant d$ for geometric consistency (as x_3 and x_2 correspond to the geometric variables b and d, respectively). This problem is classically transformed into an unconstrained optimization problem through a penalty method [52]:

$$\boldsymbol{x}_{\text{opt}} = \arg\max_{\boldsymbol{x}\in S} J(\boldsymbol{x}) + P_h(\boldsymbol{x}), \tag{37}$$

where the penalty function P_h is defined as

$$P_h(\boldsymbol{x}) = \text{sgn}(\min(\{0, h(\boldsymbol{x})\})), \tag{38}$$

and sgn denotes the sign function. The first term in the right-hand side in Eq. (37) is the initial cost function to be maximized (see Eqs. 17,18), while the second term is added to penalize nonconstrained candidates for which the inequality constraint given by Eq. (36) is not satisfied.

For the formulation detailed in Section 2, the optimization problem above is highly nonconvex [53]. It is therefore solved heuristically in this work, by using particle swarm optimization [54] (PSO) (notice that a discussion regarding optimization algorithms for general, non-convex problems is beyond the scope of this study). The stochastic approach conceptually emulates group behavior by introducing a population of potential solutions (called the swarm) randomly, and by updating these solutions in a recursive manner, according to a maximization criterion. In order to review the updating procedure, let $\boldsymbol{x}_t^i \in S$ be the position of particle i at iteration t. The velocity vector for particle i at iteration t is denoted by $\boldsymbol{v}_t^i$ and is defined as $\boldsymbol{v}_t^i = \boldsymbol{x}_t^i - \boldsymbol{x}_{t-1}^i$. Finally, let $\boldsymbol{P}_t^i$ and $\boldsymbol{G}_t$ be the i-th particle's individual best solution and the swarm best solution up to iteration t, respectively. In a basic PSO implementation, these vectors are updated for all particles as follows. First the velocity of particle i is updated according to

$$\boldsymbol{v}_{t+1}^i = \phi_t \boldsymbol{v}_t^i + \varphi_1 \boldsymbol{R}_{1t}^i \left(\boldsymbol{P}_t^i - \boldsymbol{x}_t^i\right) + \varphi_2 \boldsymbol{R}_{2t}^i (\boldsymbol{G}_t - \boldsymbol{x}_t^i), \tag{39}$$

where ϕ_t is the particle inertia introduced by Shi and Eberhart [54,55], φ_1 and φ_2 are the cognitive and social coefficients, respectively, and $\boldsymbol{R}_{1t}^i$ and $\boldsymbol{R}_{2t}^i$ are two diagonal matrices of independent random numbers following a uniform distribution on $[0, 1]$. In Eq. (39), the quantities $\left(\boldsymbol{P}_t^i - \boldsymbol{x}_t^i\right)$ and $(\boldsymbol{G}_t - \boldsymbol{x}_t^i)$ represent social and cognitive influences, respectively: these terms, weighted by their respective coefficients φ_1 and φ_2, aim to attract the particle towards pseudo-optimal solutions at the particle and swarm levels. The position and individual best solution for particle i are next updated following

$$\boldsymbol{x}_{t+1}^i = \boldsymbol{x}_t^i + \boldsymbol{v}_{t+1}^i, \tag{40}$$

and

$$\boldsymbol{P}_{t+1}^i = \begin{cases} \boldsymbol{x}_{t+1}^i & \text{if} J(\boldsymbol{x}_{t+1}^i) > J\left(\boldsymbol{P}_t^i\right) \\ \boldsymbol{P}_t^i & \text{otherwise} \end{cases}. \tag{41}$$

The SA and optimization formulations will be used, in the next section, to investigate the design of single-layer and multi-layer absorbers.

4. Results and discussion

In order to illustrate the contributions of the proposed framework, the geometries of the components (i.e., the excited PP, the air cavity, and the foam layer) in the multi-layer absorber (see Fig. 1) are selected as follows. For the foam layer, three foam configurations [19] with various geometrical parameters are introduced as listed in Table 1. The structures of the foam material in Table 1 below is taken from [19] (see P1, P2, and P3 in Table 1 in [19]). In terms of material representation, note that a SEM picture of foam sample P2 is shown in Fig. 1 (left panel) in [19]. To the authors' knowledge, SEM images of the remaining foam samples P1 and P3 are not available in the literature. One possible strategy to circumvent that limitation would consist in reconstructing the corresponding microstructures, by combining the parameters available in Table 1 with an idealized model (see Fig. 1, right panel).

For the other components of the MA configuration, the PP geometrical parameters and cavity length are selected as design parameters with admissible ranges listed in Table 2. Notice that these ranges are selected to account for manufacturing constraints and lead to a total thickness for the MA that is twice the value of L_f.

Regarding the choice of the design parameters, it is important to notice that parameters like R_w, l, and t can be accurately adjusted through advanced laboratory techniques, such as milli-fluidic techniques; see for instance [16]. Adapting these manufacturing techniques to large-scale industrial production capabilities may, however, still be an issue. One may note that alternative parameters and models have been proposed in the literature to potentially replace microstructural descriptors of the foam morphology by a suitable statistical distribution for the pore size, for instance [17].

Regarding the sensibility analyses, we consider uniform probability measures, that is, we take

$$P_{\boldsymbol{X}} = \bigotimes_{i=1}^{D} P_{X_i} \tag{42}$$

with

$$P_{X_i}(dx_i) = \frac{1}{b_i - a_i} dx_i, \quad 1 \leqslant i \leqslant D, \tag{43}$$

where $a_i = 0.95\underline{x}_i, b_i = 1.05\underline{x}_i$, and $\underline{x}_i$ is the nominal value for design parameter x_i. For the PP single-layer case, the support of the uniform distributions are listed in Table 2.

Sensitivity analysis for single-layer absorbers are first presented in Section 4.1. We subsequently perform design optimization for multi-layer absorbers in Section 4.2. Sensitivity results for the configurations thus obtained are finally provided in Section 4.3.

4.1. Sensitivity analysis for single-layer absorbers

In this section, the sensitivity analysis is performed for single-layer foam absorbers. We specifically characterize the sensitivity with respect to four parameters, namely the strut length l, the strut size t, the reticulation rate R_w, and the layer thickness L_f. Since the indices are computed through a spectral decomposition at all frequencies (using the results from Monte Carlo simulations for verification purposes), the convergence with respect to the order of the polynomial chaos expansion (which is used as the polynomial surrogate approximating the mapping between the input and output variables, as discussed at the end of Section 3.1), denoted by Q, is first analyzed. Fig. 2 shows the convergence of the statistical estimators for all indices as a function of the polynomial chaos expansion order, which is denoted by Q. For a given order Q, and following [49], coefficients in the polynomial chaos representation are evaluated with a regression method, using

$$M = k_M \frac{(D+Q)!}{Q!D!} \tag{44}$$

independent samples of the input parameters ($k_M \geqslant 2$). From Fig. 2, it is seen that reasonable convergence is obtained for $Q \geqslant 4$ (requiring $M = 140$ evaluations of the multiscale model).

Table 1
Microstructural parameters of three membrane foam samples [19].

Foam sample	Morphology factors and thickness					
	C_s[mm]	l [μm]	t [μm]	R_w	ϕ	L_f [mm]
F1	613	208	46	1.00	0.956	25.4
F2	616	209	50	0.32	0.957	25.4
F3	1710	550	149	0.05	0.971	25.4

Table 2
Admissible ranges for the PP geometrical parameters and air gap distance.

Parameter	Admissible range [mm]
PP thickness t_m	$[1, 3]$
Hole diameter d	$[1, 3]$
Hole spacing b	$[2, 8]$
Airgap distance L_a	$[5, 30]$

The evolution of the sensitivity indices over the frequency ranges can be seen in Figs. 3–5 for the three foams F1 to F3, respectively. Based on these results, we can formulate the following observations.

- For the first foam F1 (see Fig. 3), the most influential microstructural parameters are, in order, the struts length l and the thickness t. In general, the ratio l/t significantly affects the behavior of the foam. It should also be noticed that the existence of residual membranes can impact the acoustic response of the foam, through R_w. Finally, the thickness of the porous layer plays a major role for open foams with a rigid backing. In particular, the sensitivity index for L_f varies very substantially at very low frequencies ($\omega \approx 0$) where the absorption tends towards zero, and becomes smaller than the other indices at higher frequencies. It is seen that the influence of L_f is greater for wavelengths that are much greater than the quarter wavelength (that is, far away from the peak of absorption, which occurs around 4500 [Hz]). At the quarter wavelength resonance, the acoustic response, indeed, strongly depends on the boundary conditions at the rear surface of the porous sample and is thus less impacted by variations in foam thickness L_f. Beyond 4300 [Hz], the porous material is very efficient, so that the relative influence of the foam thickness L_f on the global response decreases (in contrast with the behavior at very low frequencies).
- The second foam F2 has a characteristic cell size similar to F1, but contains membranes ($R_w = 0.32$). In this case (see Fig. 4), the absorption coefficient (for normal incidence and rigid backing) is primarily dominated by the thickness L_f for the porous material. Near the quarter wavelength resonance (≈ 2300 [Hz]), the influence of L_f becomes negligible as compared to other parameters, and in particular with respect to the strut length l and reticulation rate R_w (the influence of l is predominant on the cell size and hence, on the resistivity σ at low reticulation rates).
- Overall, similar comments can be made on the third foam F3. The most influential parameter for a normal incidence sound absorption with a rigid backing is the thickness L_f, except when L_f is an integer multiple of the quarter wavelength. This influence drops substantially near the quarter wavelength resonance, for which the strut length l and the reticulation rate R_w become more important parameters. The resonances observed at one and three times the quarter wavelength correspond to configurations where the particle velocity at the front surface of the porous sample is extreme and viscous effects dominate. In contrast, the particle velocity vanishes at the front surface of the porous material when the sample thickness coincides with two times the quarter wavelength (near 2500 [Hz]). In this case, the microstructural parameters—and in particular, the parameter R_w for a foam with low reticulationrate ($R_w = 0.05$)—become more important (as compared to L_f). This highlights the benefit of foams with gradients of properties, as discussed in Ref. [23]. It can further be observed that because $\lambda_{eq}(f)$ is a complex function of frequency (as shown in Fig. 10 in Ref. [58]), the frequency at which the second peak occurs is not simply equal to three times the frequency at which the first

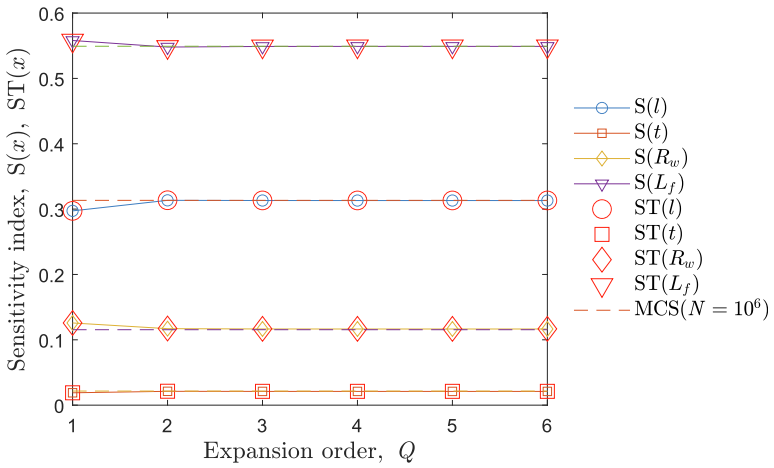

Fig. 2. Convergence of the statistical estimators of the sensitivity indices estimated at 1000 [Hz] (foam F2). Here, Q is the order of the polynomial expansion, and the dashed lines represent the sensitivity indices estimated using Monte-Carlo simulations ($N = 10^6$ samples). Following the notation introduced in Section 3.1, $\mathrm{S}(x)$ and $\mathrm{ST}(x)$ denote the normalized global and total sensitivity indices associated with variable x (see Eqs. (30) and (32), respectively). This figure shows that an order $Q \geqslant 4$ must be retained to properly estimate the sensitivity indices using the surrogate model.

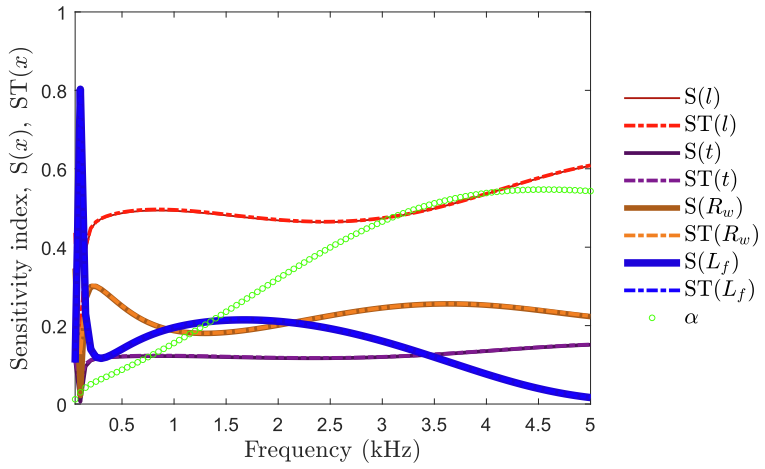

Fig. 3. First-order and total sensitivity indices for foam F1. Following the notation introduced in Section 3.1, $S(x)$ and $ST(x)$ denote the normalized global and total sensitivity indices associated with variable x (see Eqs. (30) and (32), respectively). The evolution of the sensitivity indices over the frequency range shows that l and R_w are predominant variables, except at $w \to 0$ where the foam thickness L_f becomes more influential.

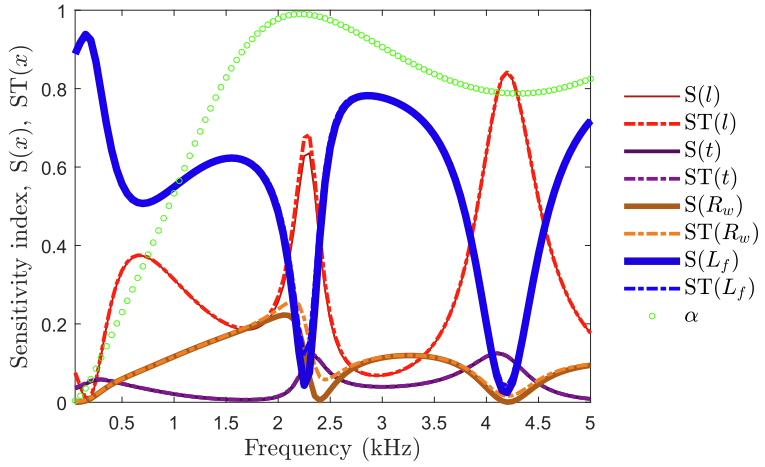

Fig. 4. First-order and total sensitivity indices for foam F2. Following the notation introduced in Section 3.1, $S(x)$ and $ST(x)$ denote the normalized global and total sensitivity indices associated with variable x (see Eqs. (30) and (32), respectively). By comparing this figure with Fig. 3, it is seen that the thickness L_f is now predominant, due to membrane effects (here, the foam behaves as a resistive layer). In the vicinity of the quarter wavelength and half wavelength resonant frequencies, the microstructural parameters l and R_w prevail again, as observed in Fig. 3.

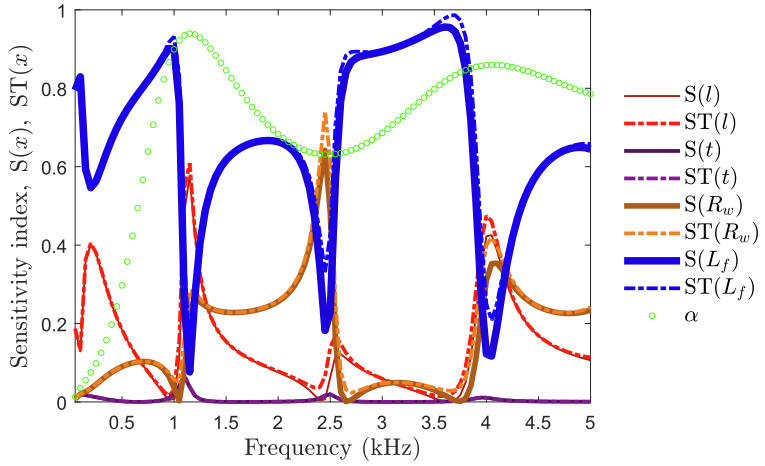

Fig. 5. First-order and total sensitivity indices for foam F3. Following the notation introduced in Section 3.1, $S(x)$ and $ST(x)$ denote the normalized global and total sensitivity indices associated with variable x (see Eqs. (30) and (32), respectively). Because the sound absorption of a porous material backed by a rigid layer is essentially controlled by the product of its resistivity σ times the corresponding thickness L_f, the dominating parameter on the overall response function is the thickness L_f for a given foam morphology (global resonance dominated by bulk effects). The relative influence of L_f declines appreciably for multiple integers of the quarter wavelength resonance; where the effects of cell size and membrane become dominant through l and R_w microstructural parameters.

peak occurs, and the frequency at which the first dip occurs is not simply equal to two times the frequency at which the first peak occurs. Indeed, the quarter wavelength resonance absorption of the porous material is governed by its intrinsic damped complex wavelength, $\lambda_{eq}(f) = \sqrt{K(f)/\rho(f)}/f$, and not the one in the air. This was also underlined in Refs. [56,57]. The first peak appears at the quarter wavelength, where $L/\Re(\lambda_{eq}(f)) = 1/4$.

These SA results are consistent with the findings in Refs. [19–21]. The first order sensitivity index of all inputs is very close to the total order ones. This indicates that the interactions of input variables in a small range can be ignored in the SA performance for acoustic models of such materials.

Then, we evaluated the sensitivity functions for the PPs backed by an air cavity in order to see how these input design factors affect the SAC under normal incidence. We are assuming that the four geometric factors are following a uniform distribution over the ranges listed in Table 2. As shown in Fig. 6, the sensitivity functions of input variables fluctuate strongly with the frequency of interest. In Fig. 6a, the results of the first-order sensitivity index reveal that factors d and b are the most influential factors in the broad low frequency range (i.e., < 3 [kHz]), whereas the length of the air gap, L_a, displays a strong impact at the remaining frequencies. We note that the latter geometric factors, b and d, could be gathered in a single non-dimensional parameter, which is the surface porosity. In Fig. 6b, the sum of the total-order indices is larger than 1.5 in the whole frequency range. This observation indicates that in contrast with previous results regarding a single foam layer (Figs. 3–5 and related comments), the interaction of input parameters must be specifically considered in the investigated range of frequencies. It can be seen from Fig. 6(a) and (b) that the sensitivity indices $\mathrm{S}(x)$ and $\mathrm{ST}(x)$ both reveal a relatively small effect of the plate thickness t_m when compared to the other variables of the design space, d, b, and L_a (in the range of constrained geometrical parameters given in Table 2). Here, the coupling between the design space variables can be attributed to the fact that a PP is essentially a Helmholtz resonator, or a mass-spring system, where the air mass is directly related to the perforations (d, b, t_m) and the stiffness of the spring linked to the air cavity (L_a). These important levels of the design variables are also investigated through the optimization procedure in the next section.

4.2. Multi-layer absorber design optimization

In this section, we consider the optimization of the mean absorption coefficient α_A (see Eq. (16), where we take $N_f = 100$, and Eq. (17) over low and high frequency ranges, specified as [200, 1500] [Hz] and [1500, 4000] [Hz], respectively.

Following the results in the previous section, where it was shown that the thickness of PP structure has less influence than the other parameters, we consider two scenarios where t_m is either integrated (in which case $D = 4$) or disregarded (i.e., $D = 3$) in the optimization process. We denote by (WiT) and (WoT) these scenarios. Multiple (WoT) analyses are conducted by selecting a value t_m^i for the thickness t_m such that $t_m^i = 1 + (i-1)/2$ [mm], with $1 \leqslant i \leqslant 5$. Relevant variables are assumed to vary within the ranges reported in Table 2.

We use the particle swarm optimization framework presented in Section 3.2 to compute the optimal parameters of PP and airgap for MA configurations. Results are reported in Table 3 and illustrated, for the (WoT) analysis, in Fig. 9. Notice that in Table 3, results obtained for the (WiT) computations are compared with the ones obtained with the (WoT) scenario, taking $t_m = t_m^3 = 2$ [mm].

In Fig. 7, we show the evolution of the cost function with respect to iteration numbers in the PSO, as well as the associated optimal SAC curves.

First, we examine the optimal configurations in the low frequency range [200, 1500] [Hz], for the different foam layers (MA1-MA3), Fig. 7b. At high reticulation rate ($R_w = 1$), visco-thermal losses are relatively low (Foam layer F1), and only a Helmholtz resonator partially filled with the open cell structure can absorb sound energy in this low frequency range (MA1, with a peak of absorption around 800 [Hz], and visco-thermal dissipation of the open-cell foam for larger frequencies). The quarter wavelength resonance of the partially open-cell foam ($R_w = 0.32$) is about 2000 [Hz] (Foam layer F2), a value larger than the aimed frequency range [200, 1500] [Hz]; both effects effectively increase sound absorption in the frequency range of interest. A Helmholtz resonator is therefore still necessary to tackle the low frequency range of interest. The visco-thermal dissipations of the porous material (Foams layer 2) enable to significantly increase the overall efficiency of the multi layer absorber (MA2) above the low frequency absorption peak (due to the Helmholtz resonator). The third resistive layer of foam (Foam layer F3, $R_w = 0.05$) already exhibit a peak of absorption (around 1000 [Hz]) in the frequency range of interest [200, 1500] [Hz]. The associated optimal configuration consists in a first peak of absorption due to a Helmholtz resonance (around 800 [Hz]) coupled with quarter wavelength resonance (around 1500 [Hz]) resulting in a large band of high sound absorption. Interestingly, the quarter wavelength resonance of the (equivalent) porous material (Foam layer F3 with the corresponding air gap, around 1100 [Hz]) has been shifted towards a higher frequency (around 1500 [Hz]).

We note that the admissible range of values for the hole diameter, d in [1,3] [mm] imposes a strong constraint, the resistance of

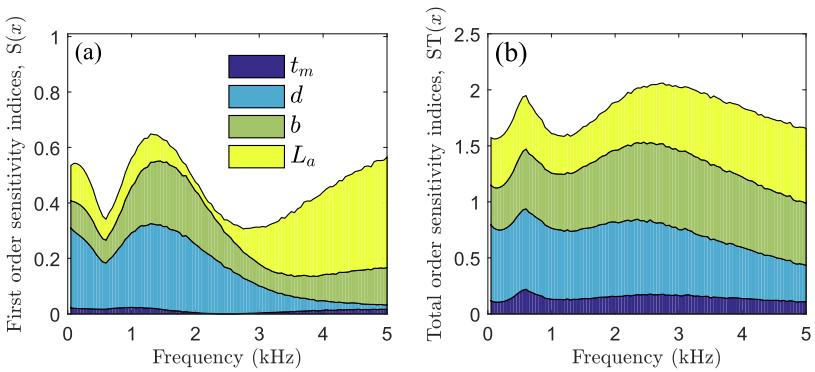

Fig. 6. Area plots of the (a) first- and (b) total-order sensitivity indices of the PPs backed an air cavity. The results shown here were obtained for a polynomial order $Q = 8$ and $M = 12375$.

Table 3
Optimal values for design parameters of PP and airgap for MA configurations. Results for the (WoT) case are obtained using a thickness $t_m = t_m^3 = 2$ [mm].

Configuration	Foam	Freq. range [Hz]	PP structure			Airgap
			t_m [mm]	d [mm]	b [mm]	L_a [mm]
			WiT	WiT (WoT)	WiT (WoT)	WiT (WoT)
MA1	F1	[200, 1500]	1.00	1.00 (1.00)	6.31 (5.04)	5.0 (5.0)
MA2	F2	[200, 1500]	1.00	1.00 (1.00)	4.99 (3.98)	5.0 (5.0)
MA3	F3	[200, 1500]	1.00	1.00 (1.00)	2.86 (3.36)	25.9 (25.9)
MA4	F1	[1500, 4000]	3.00	1.00 (1.00)	2.48 (2.20)	30.0 (30.0)
MA5	F2	[1500, 4000]	1.00	1.13 (1.46)	2.00 (2.00)	13.6 (13.5)
MA6	F3	[1500, 4000]	2.22	1.00 (1.00)	2.11 (2.19)	8.4 (8.0)

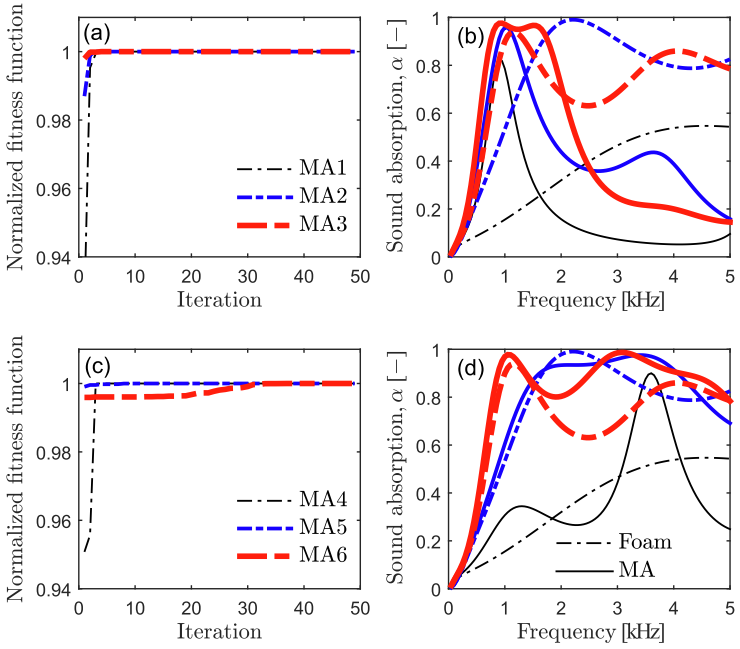

Fig. 7. PSO normalized fitness function(a,c) and sound absorption coefficient for the optimal MAs (solid lines) and original foam layers (dashed lines) (c,d). Results in (a,b) and (c,d) are obtained by maximizing the SAC at low and high frequencies, respectively.

the perforated plate (the product of the resistivity of the perforated plate and its thickness) corresponds to a value too low for the perforated plate to be optimal [60], see Eq. (10).

In the frequency range [1500, 4000] [Hz], the quarter wavelength resonances are still observed, but the Helmholtz resonance are shifted towards higher frequencies—in order to obtain a wideband resonator in the target frequency range (see the panel (d) in Fig. 7). It should be noticed that other designs could lead to similar behavior, including (i) a solution where the perforation ratio is increased and the perforation hole diameter decreased (so that the resistivity is adapted to air characteristic impedance), and (ii) a scenario where the thickness of the porous medium is decreased in order to shift the quarter wavelength towards the desired frequency range [60].

Fig. 8 shows how the sound absorption varies for each configuration (MA1-MA6) when a modification of the plate thickness is imposed (t_m) in the constrained range of admissible values [1,3] [mm]. We note that the values of d and b (governing the perforation ratio) are adapted to keep the maximized sound absorption (in the frequency ranges of interest); see Fig. 9.

Table 4 shows that this effect is not significant when considering the overall sound absorption average, α_A. A detailed analysis of Fig. 7 shows, however, that a selection of a specific optimal design may be done within the obtained set (t_m, d, b, L_m) to favor specific parts of the absorption spectrum.

It can be seen from Fig. 7 and Table 4 that the multi-layer configuration provides a clear improvement as compared to single foams:

- For a low-frequency target, a peak of sound absorption with a magnitude larger than 0.9 can be obtained in the middle of the frequency range, except for sample MA1 for which a slightly lower value of 0.8 is observed (notice that in this case, the average sound absorption obtained for MA1 is three times greater than the one for the foam; see the first line in Table 4);
- For a high-frequency target, we also obtained a wideband sound absorption $\alpha_A > 0.9$, and $\alpha > 0.8$ over the whole frequency range (that is, [1500 4000] [Hz]) for configurations MA5 and MA6.

In order to illustrate the PSO framework, the evolution of the positions for a swarm having 50 particles is shown below, in Fig. 10. Here we consider the maximization of the mean sound absorption coefficient α_A as a function of the design parameters t_m, d, b, and L_a. The plots correspond to the configurations MA3 (top panels) and MA6 (bottom panels) in the (WoT) scenario (i.e., $t_m = 2$ [mm]). For representation purposes, we set $d = 1$ [mm] (which is the optimal value for d, see Table 3), and we plot the graph of the function $(b, L_a) \mapsto \alpha_A(b, L_a)$. As shown in the far right panels (see Fig. 10 (c,f)), all particles in the swarm have converged

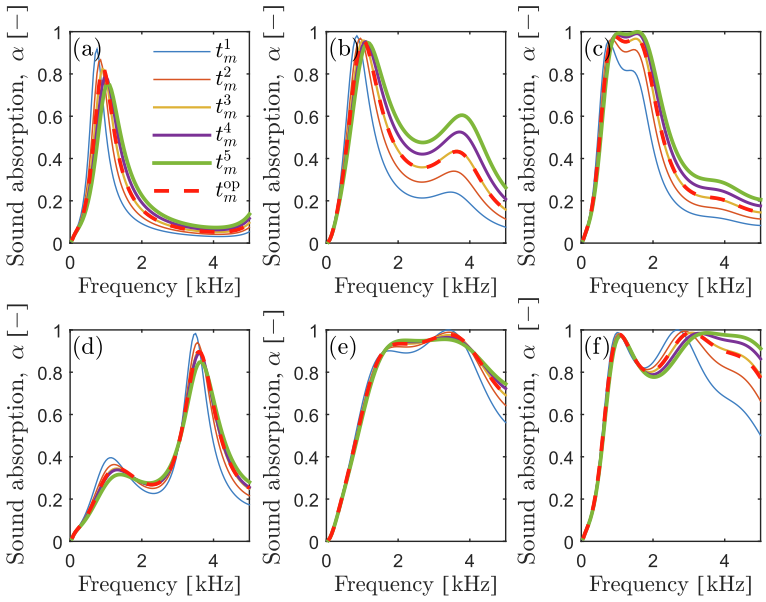

Fig. 8. Sound absorption property for optimal MAs with different PP structures: (a) foam F1, with a maximization at low frequencies; (b) foam F2, with a maximization at low frequencies; (c) foam F3, with a maximization at low frequencies; (a) foam F1, with a maximization at high frequencies; (b) foam F2, with a maximization at high frequencies; (c) foam F3, with a maximization at high frequencies.

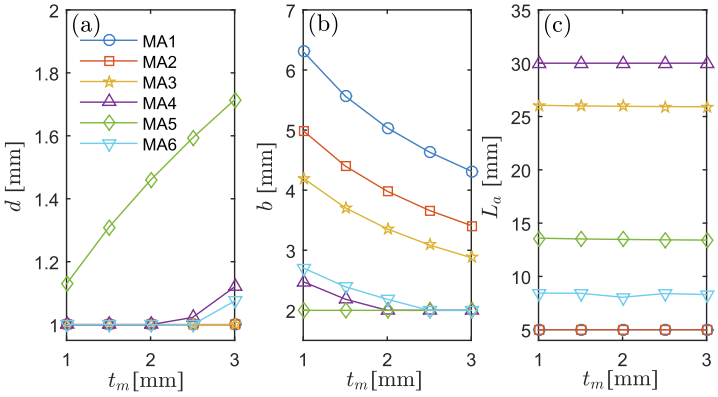

Fig. 9. Optimal values of design parameters for the (WoT) scenarios: (a) evolution of the hole diameter d as a function of the thickness of the perforated panel t_m; (b) evolution of the hole spacing b as a function of t_m; (c) evolution of the airgap thickness L_a as a function of t_m.

Table 4
Comparison of the optimal average SAC of MA absorbers and the original ones of the foam single foam layers.

Freq. range [Hz]	Average sound absorption, α_A [-]						
	Foam	MA (WiT, t_m^{op})	MA (t_m^1)	MA (t_m^2)	MA (t_m^3)	MA (t_m^4)	MA (t_m^5)
[200, 1500]	0.1372 (F1)	0.4664	0.4664	0.4647	0.4637	0.4629	0.4624
[200, 1500]	0.4430 (F2)	0.6435	0.6435	0.6433	0.6431	0.6430	0.6429
[200, 1500]	0.6275 (F3)	0.7454	0.7452	0.7453	0.7453	0.7454	0.7454
[1500, 4000]	0.3803 (F1)	0.4781	0.4781	0.4773	0.4767	0.4736	0.4700
[1500, 4000]	0.8674 (F2)	0.9440	0.9440	0.9435	0.9432	0.9429	0.9427
[1500, 4000]	0.7584 (F3)	0.9018	0.9017	0.9017	0.9015	0.9018	0.9014

to the global optimum locations at the final iteration, for both optimization processes.

4.3. Sensitivity analysis for optimized multi-layer absorbers

In this section, sensitivity analysis for acoustic models is performed for the optimal MA configurations defined in Table 1 and Table 3. Due to the small impact of the PP thickness on the sound absorbing behavior of MA absorbers (in the frequency ranges of interest), this parameter is omitted in the SA computations. We therefore consider a total of seven geometric input variables, including four factors related to the foam layer (namely, l, t, R_w, and L_f, as described in Section 4.2) and three other parameters related to the structural configuration (namely, the perforated characteristics of the PP, d and b, and the air gap thickness, L_a). We recall that these input parameters are defined by Eq. (43) with the nominal values listed in Table 1 and Table 3. As in Section 4.1, we first conduct a convergence analysis to ensure that the sensitiv-

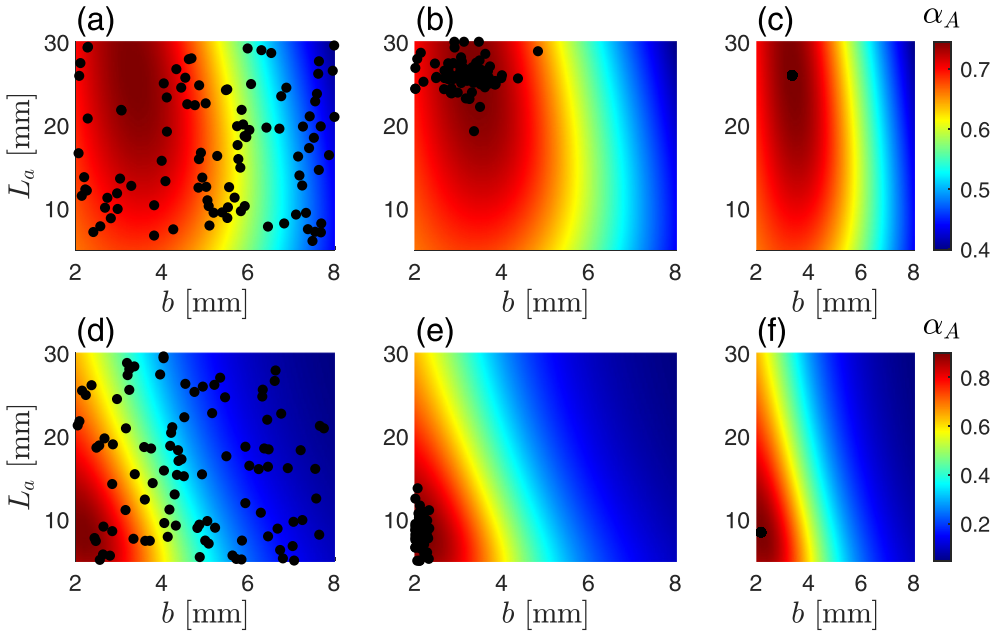

Fig. 10. Evolution of the positions (black solid markers) for a swarm having 50 particles. Here we seek to optimize the mean sound absorption coefficient α_A as a function of t_m, d, b, and L_a. For representation purposes, we set $t_m = 2$ [mm] and $d = 1$ [mm], and consider b and L_a as design variables. The following results are displayed: (a,c) initial positions for the swarm, (b,e) positions at the 15^{th} iteration, and (c,f) final positions for the swarm (at the 50^{th} iteration). For the MA3 configuration (top panels), the global maximum is located at $\boldsymbol{x}^* = [3.3625.9]$ and corresponds to $\alpha_A^{\max} = \alpha_A(\boldsymbol{x}^*) = 0.7453$. For the MA6 configuration (bottom panels), the global maximum is located at $\boldsymbol{x}^* = [2.198.0]$ and corresponds to $\alpha_A^{\max} = \alpha_A(\boldsymbol{x}^*) = 0.9015$.

ity indices are properly estimated through the spectral expansion approach. Results are presented in Fig. 11 for a specific configuration, namely MA2. It is seen that selecting $Q = 4$ (corresponding to only 660 evaluations of the multiscale model) provides reasonably well converged estimates for the sensitivity indices.

The results of the sensitivity analysis are illustrated in Fig. 12 and Fig. 13. These results are in accord with the observation that the impact of the input geometric parameters on the sound absorbing coefficients strongly depends on both (i) the absorber microstructure and (ii) the considered frequency range of interest. The coupling effects between input parameters occur mainly at the frequency of the sound absorption peaks as demonstrated by total order effects larger than 1. The results reveal a difference in the impact levels of input parameters before a resonance frequency, for a resonance frequency, and after a resonance frequency.

For the multi-layer absorber configurations MA1 to MA3 for the low frequency target (i.e., in the range [200, 1500] [Hz]), the size and the spacing of the holes (i.e., d, b), and the foam layer thickness (L_f) dominate on the impact of the variability of the sound absorption coefficient in the whole frequency range, since they respectively control the selectivity of the Helmholtz resonance and the quarter wavelength resonance (see Sections 4.1 and 4.2). At frequencies around the first SAC peak, the strut length parameter in foam materials is a key parameter for highly reticulated foams

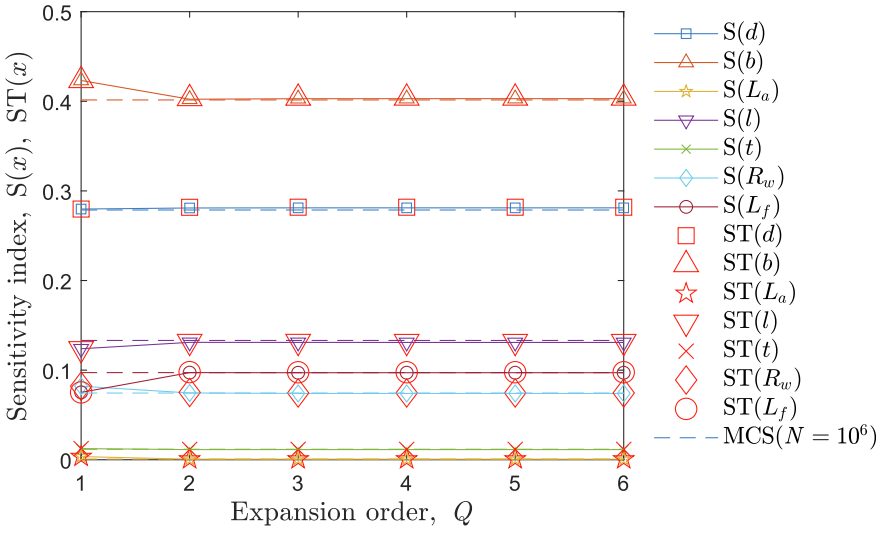

Fig. 11. Sensitivity indices at frequency of 2500 [Hz] with different values of expansion order Q for configuration MA2. The dashed lines correspond to the sensitivity indices estimated with the Monte Carlo approach (with sample size $N = 10^6$). Following the notation introduced in Section 3.1, S(x) and ST(x) denote the normalized global and total sensitivity indices associated with variable x (see Eqs. (30) and (32), respectively).

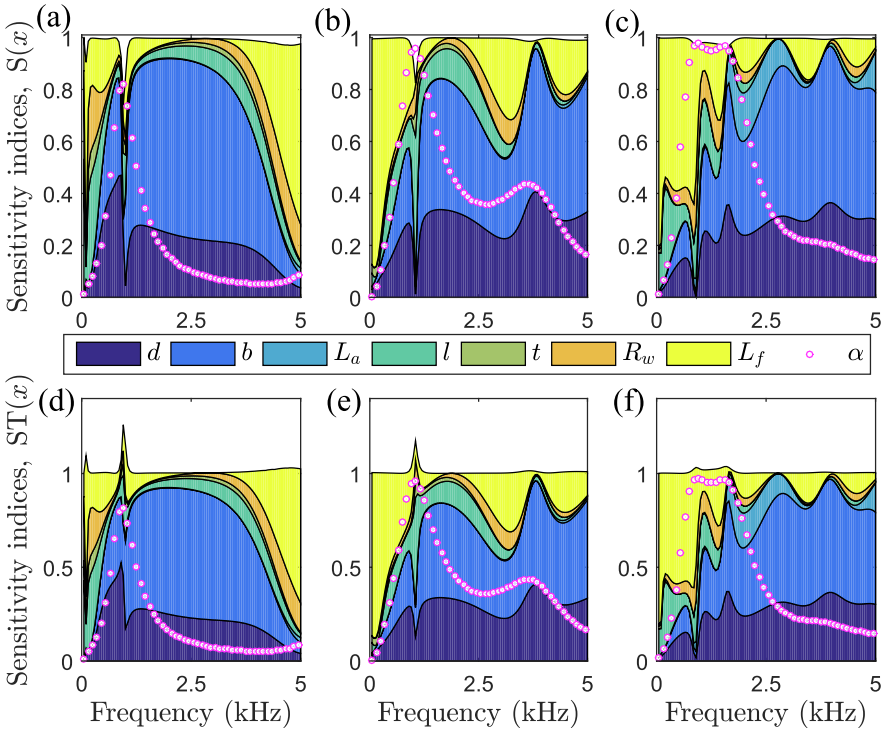

Fig. 12. Area plots for sensitivity indices: (a) first-order indices for sample MA1; (b) first-order indices for sample MA2; (c) first-order indices for sample MA3; (d) total indices for sample MA1; (e) total indices for sample MA2; (f) total indices for sample MA3.

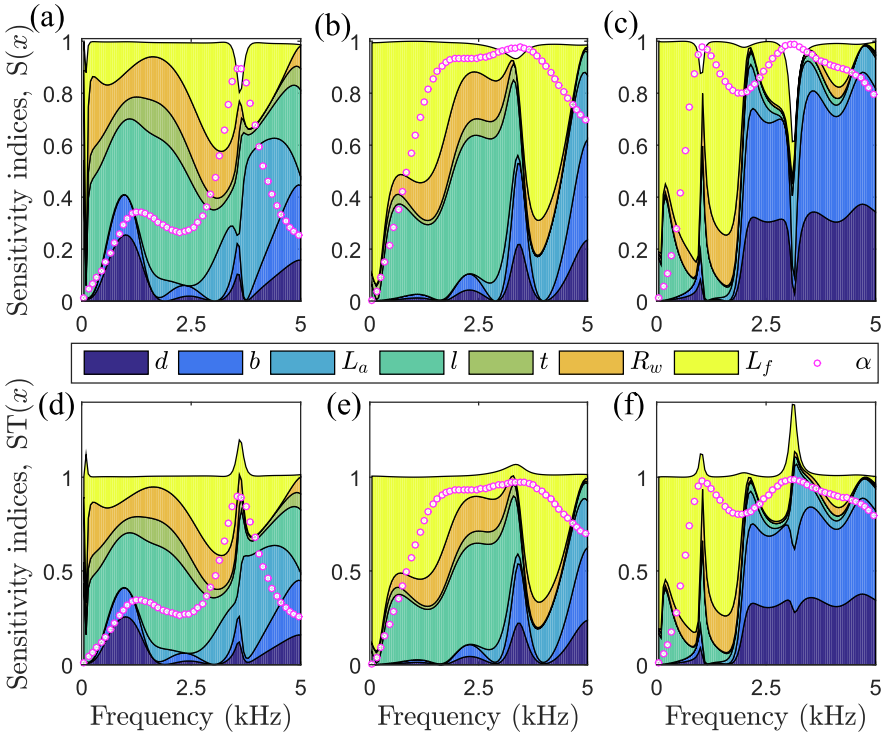

Fig. 13. Area plots for sensitivity indices: (a) first-order indices for sample MA4; (b) first-order indices for sample MA5; (c) first-order indices for sample MA6; (d) total indices for sample MA4; (e) total indices for sample MA5; (f) total indices for sample MA6.

(i.e., $R_w > 0.32$) due to its strong impact on the internal visco-thermal dissipations of the foams through the porosity and the resistivity, [Eqs. (5)–(9)], (see Fig. 12a-b with the sensitivity indices around 0.4 for the strut length parameter). For the configuration MA3 based on a more resistive and tortuous foam sample with a low reticulation rate (i.e., $R_w = 0.05$) [Eqs. 8,9], the sound absorption coefficient is highly impacted by the foam thickness (L_f, with its sensitivity indices greater than 0.5) in particular at frequencies

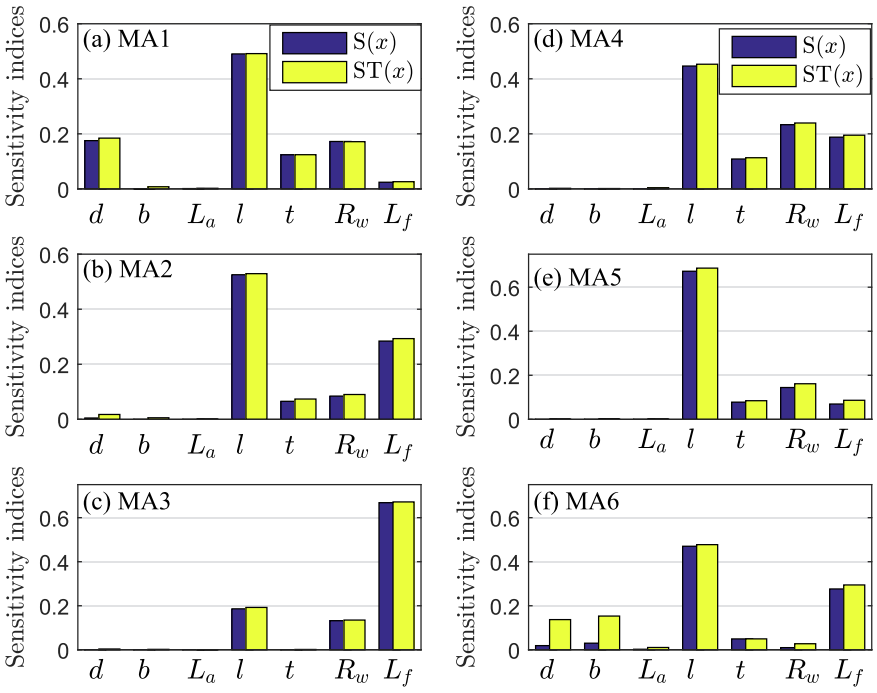

Fig. 14. First-order and total sensitivity indices for α_A: (a) sample MA1; (b) sample MA2; (c) sample MA3; (d) sample MA4; (e) sample MA5; (f) sample MA6.

lower than the first SAC peak (i.e., $f < 1$[kHz]); since the foam layer thickness controls the quarter wavelength resonance which is here coupled with the Helmholtz resonance.

With the absorbers MA4 to MA6 in the frequency range of interest [1500, 4000] [Hz], sensitivity functions of input variables of the foam layer (l, t, L_f) display a similar behavior to the one reported for the frequency range of interest [200, 1500] [Hz]. However, because the second sound absorption peak is somehow correlated to a quarter wavelength resonance of the foam sample, the microstructural descriptors of the porous layer together with the foam layer thickness have a strong impact on a large frequency range, i. e. [0, 4000] [Hz]. As expected for the MA4 configuration, the SAC variability is also affected by the PP parameters (d, b) around 1200 [Hz] due to the Helmholtz resonance. Likewise, strong effects of (d, b) in the vicinity of the second peaks of the SAC for MA5 and MA6 confirm that they are due to a Helmholtz resonance. In addition, Fig. 13f reveals the significant effect of the Helmholtz resonator (b, d, L_a) on the SAC in a wide frequency band [2000, 5000] [Hz], MA6 configuration. We see that pronounced visco-thermal dissipations are already occurring (3/4 wavelength resonance) around 4200 [Hz] (see Fig. 7d, MA6). Visco-thermal losses are then coupled with the Helmholtz resonator design ("holes" or internal ducts and cavity of the equivalent "mass-spring" system; see also Ref. [59]). Therefore, adding a perforated panel with a cavity to the visco-thermal losses provided by the foam layer leads to an enhancement of the SAC in the range of frequencies [0, 4000] [Hz]. Noticeably, the forced sound absorption peak around 3800 [Hz] also results from a modification of the effective bulk modulus of the medium. Fig. 13 equally shows that the resistive foam layer is specifically influenced by the microstructural characteristics (l, R_w, t). We see that, in the configuration MA5, the perforation ratio is large compared to the other configurations (around 25 %); this reduces the levels of the sound absorption peaks, but increases the overall sound absorption in a large frequency range (at least 1800 [Hz] to 4800 [Hz])—see for instance Ref. [60].

Here we considered the output of α_A computed with a number of frequencies $N_f = 100$ for both the "low" frequency target and the "high" frequency target. Fig. 14 shows SA results for MA configurations studied in Fig. 12 and Fig. 13. Generally, the values of the first sensitivity index are very close to those of the total one. This suggests that at the leading order, the interaction effects of the input parameters on the output metric can be neglected (as previously discussed). Once the geometrical parameters of the resonator (namely, d, b, and L_a) have been determined by the optimization algorithm, the local resonating behavior effect provided by the Helmholtz resonator is robust. Moreover, the interaction with the global quarter wavelength resonance strongly depends on the intrinsic properties and thus, on the microstructural features (l, t, R_w, and L_f) of the porous layer itself. This statement has to be hampered when the visco-thermal dissipations provided by the porous substrate are low (MA1) or when local and global resonances closely interact (MA6).

5. Conclusion

The design of porous layers under sound absorption constraints was investigated using variance-based sensitivity analysis, conducted through a spectral decomposition for enhanced computational efficiency, and non-convex particle swarm optimization. From a practical standpoint, the methodology can be used to identify the most influential parameters within the multiscale setting, hence enabling (i) robust design when design parameters are considered uncertain, and (ii) optimization in a lower dimensional space (disregarding variables that have negligible impacts on the quantities of interest). The inner layers of the multi-absorber configuration including a micro-perforated panel and a foam layer, as well as air depth, are specifically tuned to maximize sound absorption at normal incidence in specific frequency ranges. The following conclusions can be drawn from the sensitivity and optimization results.

1. For foam-based absorbers without membranes, the most influential microstructural parameter is generally the strut length (which has a predominant effect on the resistivity), in accordance with results provided elsewhere.

2. In the case of foams having a membrane content, the layer thickness is the most influential factor for a sound absorption at normal incidence with a rigid backing (bulk effect), except when the frequency is a integer multiple of the quarter-wavelength resonant frequencies (where, for a given porous sample thickness, the microstructural parameters influencing resistivity play a major role).
3. The sensitivity indices related to the geometrical parameters of the multi-layer absorbers strongly depend on the properties of the porous layer. In frequency-dependent terms, both the main and the total effects vary substantially in the whole frequency range of interest, and interaction effects between input variables occur essentially around the local resonance frequencies (Helmholtz resonator).
4. The sound absorption response typically exhibits two peaks related to Helmholtz and quarter-wavelength resonances, respectively. The role of the geometrical factors for the micro-perforated panel and cavity depth essentially consists in shifting and amplifying both of these resonances such that they can occur in the frequency range of interest. Once robust design is achieved in terms of these design factors, the microstructural parameters in the porous layer become the predominant factors.

Possible avenues for further research include:

(i) the consideration of multi-layer composite systems, such as multi-layer (micro-) perforated panels or multi-layer porous materials, with extended admissible ranges (especially with regards to geometrical parameters such as the perforation ratio and diameter for the perforated panels) or an increased number of input variables (including, for instance, the microstructural parameters of the porous layer, for a large range of corresponding porosity);
(ii) the modeling of sound absorption in diffuse fields;
(iii) robust design under uncertainty;
(iv) the study of sound transmission loss including elastic and/or hole interaction effects in the overall frequency-dependent response functions.

Data Availability

Data can be made available upon request.

Declaration of Competing Interest

The authors declare that they have no known competing financial interests or personal relationships that could have appeared to influence the work reported in this paper.

Acknowledgments

This work was funded by the Vietnam National Foundation for Science and Technology Development (NAFOSTED) under Grant No. 107.01–2019.316. The authors would like to thank F. Chevillotte for instructive comments and discussions about the effect of upstream resistive layers on porous materials. The contribution of the reviewers is also gratefully acknowledged.

References

[1] M.A. Biot, Theory of propagation of elastic waves in a fluid-saturated porous solid. I. Low-frequency range, J. Acoust. Soc. Am. 28 (2) (1956) 168–178.
[2] M.A. Biot, Theory of propagation of elastic waves in a fluid-saturated porous solid. II. Higher frequency range, J. Acoust. Soc. Am. 28 (2) (1956) 179–191.
[3] D.L. Johnson, J. Koplik, R. Dashen, Theory of dynamic permeability and tortuosity in fluid-saturated porous media, J. Fluid Mech. 176 (1) (1987) 379–402.
[4] D. Lafarge, P. Lemarinier, J.F. Allard, V. Tarnow, Dynamic compressibility of air in porous structures at audible frequencies, J. Acoust. Soc. Am. 102 (4) (1997) 1995–2006.
[5] T. Bourbie, O. Coussy, B. Zinszner, Acoustics of porous media, United States (1987).
[6] D.L. Johnson, Theory of frequency dependent acoustics in patchy-saturated porous media, J. Acoust. Soc. Am. 110 (2) (2001) 682–694.
[7] Y. Champoux, J.F. Allard, Dynamic tortuosity and bulk modulus in air-saturated porous media, J. Appl. Phys. 70 (4) (1991) 1975–1979.
[8] J.L. Auriault, E. Sánchez-Palencia, Etude du comportement macroscopique d'un milieu poreux saturé déformable, J. de Mec. 16 (1977) 575–603.
[9] E. Sánchez-Palencia, Homogenization in elasticity and electromagnetism, Non-homogeneous media and vibration theory, (1980), Lecture notes in physics.
[10] J.L. Auriault, Dynamic behaviour of a porous medium saturated by a newtonian fluid, Int. J. Eng. Sci. 18 (1980) 775–785.
[11] I. Malinouskaya, V. Mourzenko, J.-F. Thovert, P. Adler, Wave propagation through saturated porous media, Phys. Rev. E 77 (2008) 066302.
[12] C. Boutin, C. Geindreau, Periodic homogenization and consistent estimates of transport parameters through sphere and polyhedron packings in the whole porosity range, Phys. Rev. E 82 (2010) 18.
[13] K. Gao, J.A.W. van Dommelen, M.G.D. Geers, Microstructure characterization and homogenization of acoustic polyurethane foams: Measurements and simulations, Int. J. Solids Struct. 100–101 (2016) 536–546.
[14] J. Park, S.H. Yang, K.S. Minn, C.B. Yu, S.Y. Pak, Y.S. Song, J.R. Youn, Design and numerical analysis of syntactic hybrid foam for superior sound absorption, Mater. Des. 142 (2018) 212–220.
[15] S. Deshmukh, H. Ronge, S. Ramamoorthy, Design of periodic foam structures for acoustic applications: Concept, parametric study and experimental validation, Mater. Des. 175 (2019) 107830.
[16] V.H. Trinh, V. Langlois, J. Guilleminot, C. Perrot, Y. Khidas, O. Pitois, Tuning membrane content of sound absorbing cellular foams: Fabrication, experimental evidence and multiscale numerical simulations, Mater. Des. 162 (2018) 345–361.
[17] K.V. Horoshenkov, A. Hurrell, J.P. Groby, A three-parameter analytical model for the acoustical properties of porous media, J. Acoust. Soc. Am. 145 (4) (2019) 2512–2517.
[18] O. Doutres, N. Atalla, K. Dong, Effect of the microstructure closed pore content on the acoustic behavior of polyurethane foams, J. Appl. Phys. 110 (2011).
[19] O. Doutres, N. Atalla, K. Dong, A semi-phenomenological model to predict the acoustic behavior of fully and partially reticulated polyurethane foams, J. Appl. Phys. 113 (5) (2013) 054901.
[20] M. Ouisse, M. Ichchou, S. Chedly, M. Collet, On the sensitivity analysis of porous material models, J. Sound Vib. 331 (24) (2012) 5292–5308.
[21] O. Doutres, M. Ouisse, N. Atalla, M. Ichchou, Impact of the irregular microgeometry of polyurethane foam on the macroscopic acoustic behavior predicted by a unit-cell model, J. Acoust. Soc. Am. 136 (4) (2014) 1666–1681.
[22] W. Chai, J.L. Christen, A.M. Zine, M. Ichchou, Sensitivity analysis of a sound absorption model with correlated inputs, J. Sound Vib. 394 (2017) 75–89.
[23] J. Boulvert, T. Cavalieri, J. Costa-Baptista, L. Schwan, V. Romero-García, G. Gabard, E.R. Fotsing, A. Ross, J. Mardjono, J.P. Groby, Optimally graded porous material for broadband perfect absorption of sound, J. Appl. Phys. 126 (17) (2019) 175101.
[24] T. Cavalieri, J. Boulvert, G. Gabard, V. Romero-Garcia, M. Escouflaire, J. Regnard, J.P. Groby, Graded and anisotropic porous materials for broadband and angular maximal acoustic absorption, Mater. 13 (2020).
[25] J. Boulvert, J. Costa-Baptista, T. Cavalieri, V. Romero-Garcia, G. Gabard, E.R. Fotsing, A. Ross, M. Perna, J. Mardjono, J.P. Groby, Folded metaporous material for sub-wavelength and broadband perfect sound absorption, Appl. Phys. Lett. 117 (25) (2020) 251902.
[26] L. Barguet, V. Romero-Garcia, N. Jimenez, L.M. Garcia-Raffi, V.J. Sanchez-Morcillo, J.P. Groby, Natural sonic crystal absorber constituted of seagrass (Posidonia Oceanica) fibrous spheres, Sci. Rep. 11 (2021) 8.
[27] J. Allard, N. Atalla, Propagation of sound in porous media: modelling sound absorbing materials, 2nd ed., John Wiley & Sons, Chichester, 2009.
[28] M. Yang, S. Chen, C. Fu, P. Sheng, Optimal sound-absorbing structures. Materials Horizons 4 (4) (2017) 673–680.
[29] N. Jiménez, V. Romero-García, V. Pagneux, J.P. Groby, Rainbow-trapping absorbers: Broadband, perfect and asymmetric sound absorption by subwavelength panels for transmission problems, Sci. Rep. 7 (1) (2017) 1–12.
[30] H. Duan, X. Shen, F. Yang, P. Bai, X. Lou, Z. Li, Parameter optimization for composite structures of microperforated panel and porous metal for optimal sound absorption performance, Appl. Sci. 9 (22) (2019) 4798.
[31] Z. Liu, J. Zhan, M. Fard, J.L. Davy, Acoustic properties of multilayer sound absorbers with a 3D printed micro-perforated panel, Appl. Acoust. 121 (2017) 25–32.
[32] C. Maury, T. Bravo, Wideband sound absorption and transmission through micro-capillary plates: Modelling and experimental validation, J. Sound Vib. 478 (2020) 115356.
[33] J. Ning, Q. Geng, M. Arunkumar, Y. Li, Wide absorption bandwidth of a light composite absorber based on micro-perforated sandwich panel, Appl. Acoust. 174 (2021) 107735.

[34] H. Shao, J. He, J. Zhu, G. Chen, H. He, Low-frequency sound absorption of a tunable multilayer composite structure, J. Vib. Control (2021). 10775463211008279.
[35] R. Ghanem, D. Higdon, H. Owhadi, Handbook of uncertainty quantification, Springer, Cham, Switzerland, 2017.
[36] L. Bouazizi, H. Trabelsi, C. Othmani, M. Taktak, M. Chaabane, M. Haddar, Uncertainty and sensitivity analysis of porous materials acoustic behavior, Appl. Acoust. 144 (2019) 64–70.
[37] J.L. Christen, M. Ichchou, B. Troclet, O. Bareille, M. Ouisse, Global sensitivity analysis of analytical vibroacoustic transmission models, J. Sound Vib. 368 (2016) 121–134.
[38] S.H. Sohrabi, M.J. Ketabdari, Stochastic modeling and sensitivity analysis of underwater sound absorber rubber coating, Appl. Acoust. 164 (2020) 1072820.
[39] L. Jaouen, F. Chevillotte, Length correction of 2D discontinuities or perforations at large wavelengths and for linear acoustics, Acta Acust united Ac. 104 (2) (2018) 243–250.
[40] D.Y. Maa, General theory and design of microperforated-panel absorbers, ACTA ACUSTICA-PEKING. 22 (1997) 385–393.
[41] D.Y. Maa, Potential of microperforated panel absorber, J. Acoust. Soc. Am. 104 (5) (1998) 2861–2866.
[42] Lord Rayleigh, Theory of Sound II, MacMillan, New York, 1929.
[43] I.B. Crandall, Theory of Vibration System and Sound, Van Nostrand, New York, 1926.
[44] K. Verdière, R. Panneton, S. Elkoun, T. Dupont, P. Leclaire, Transfer matrix method applied to the parallel assembly of sound absorbing materials, J. Acoust. Soc. Am. 134 (6) (2013) 4648–4658.
[45] A.B. Owen, Variance components and generalized Sobol' indices, SIAM/ASA J. Uncertain. 1 (2013) 19–41.
[46] I.M. Sobol', Sensitivity estimates for nonlinear mathematical models, Math. Model. Comput. Exp. 1 (4) (1993) 407–414.
[47] A. Saltelli, S. Tarantola, On the relative importance of input factors in mathematical models: safety assessment for nuclear waste disposal, J. Am. Stat. Assoc. 97 (459) (2002) 702–709.
[48] A. Saltelli, M. Ratto, T. Andres, F. Campolongo, J. Cariboni, D. Gatelli, M. Saisana, S. Tarantola, Global sensitivity analysis: the primer, John Wiley & Sons, 2008.
[49] B. Sudret, Global sensitivity analysis using polynomial chaos expansions, Reliab. Eng. Syst. Safety. 93 (2008) 964–979.
[50] X. Luo, Z. Lu, X. Xu, Non-parametric kernel estimation for the ANOVA decomposition and sensitivity analysis, Reliab. Eng. Syst. Safety. 130 (2014) 140–148.
[51] M. Arnst, C. Soize, K. Bulthuis, Computation of Sobol indices in global sensitivity analysis from small data sets by probabilistic learning on manifolds, Int. J. Uncertain. Quantif. 11 (2) (2020) 1–23.
[52] K. Masuda, K. Kenzo, E. Aiyoshi, A penalty approach to handle inequality constraints in particle swarm optimization, 2010 IEEE International Conference on Systems, IEEE, 2010.
[53] R. Gao, Y. Zhang, D. Kennedy, Topology optimization of sound absorbing layer for the mid-frequency vibration of vibro-acoustic systems, Struct. Multidiscipl. Optim. 59 (5) (2019) 1733–1746.
[54] J. Kennedy, R. Eberhart, Particle swarm optimization, in Proceedings of ICNN'95-International Conference on Neural Networks 4 (1995) 1942–1948.
[55] Y. Shi, R. Eberhart, A modified particle swarm optimizer, IEEE international conference on evolutionary computation proceedings, IEEE world congress on computational intelligence 1998 (1998) 69–73.
[56] V.V. Voronina, K.V. Horoshenkov, Acoustic properties of unconsolidated granular mixes, Appl. Acoust. 65 (7) (2004) 673–691.
[57] V.D. Vu, R. Panneton, R. Gagné, Prediction of effective properties and sound absorption of random close packings of monodisperse spherical particles: Multiscale approach, J. Acoust. Soc. Am. 145 (6) (2019) 3606–3624.
[58] T.G. Zieliński, R. Venegas, C. Perrot, M. Červenka, F. Chevillotte, K. Attenborough, Benchmarks for microstructure-based modelling of sound absorbing rigid-frame porous media, J. Sound Vib. 483 (2020) 115441.
[59] C. Boutin, F.X. Becot, Theory and experiments on poro-acoustics with inner resonators, Wave Motion 54 (2015) 76–99.
[60] F. Chevillotte, Controlling sound absorption by an upstream resistive layer, Appl. Acoust. 73 (1) (2012) 56–60.